# On the structure and microstructure of "PbCrO₃"

Ángel M. Arévalo-López, Miguel Á. Alario-Franco*

*Departamento de Química Inorgánica, Facultad de Químicas, Universidad Complutense de Madrid, 28040 Madrid, Spain*

## Abstract

The reliability factors of a Rietveld X-ray powder refinement of $PbCrO_3$ could be improved by considering the lead ion in a multi-minimum potential displaced from its special position. These studies coupled to EDX analysis show a certain lead deficiency. Electron diffraction and high-resolution electron microscopy reveal that the microstructure of this material is a rather complex perovskite superstructure that presents a compositional modulation, within a microdomain distribution. The proposed supercell is $\sim a_p \times 3a_p \times (\approx 14 - 18)a_p$.
© 2007 Elsevier Inc. All rights reserved.

*Keywords:* $PbCrO_3$; Perovskite; High pressure; Cation deficiency; Modulated structure

## 1. Introduction

$PbCrO_3$ perovskite was first synthesized by Roth and deVries in the late 1960s [1]. High pressure and temperature is a necessary synthesis condition in order to preserve $Cr^{4+}$ ($d^2$ state) in an octahedral environment and, thus to stabilize $PbCrO_3$. The need of high pressure as a result of the thermodynamic (in)stability of $CrO_2$, which at room pressure in air, decomposes at $\sim 623 K$, but can only be formed under high pressure [2]. Under this condition, $PbCrO_3$ is stable above a pressure–temperature line from about 50 kbars at 1023 K to 60 kbars at 1723 K, although it is commonly accompanied by some impurities. Single-crystal and powder X-ray diffraction (XRD) studies at room temperature show a cubic structure (S.G. $Pm\bar{3}m$) with constant lattice $a \approx 4.00$ Å [1]. Furthermore, by means of neutron diffraction studies at 77 and 4.2 K, Roth and deVries found that this compound shows an antiferromagnetic $G$-type structure ($a_{mag} = 2a_{nucl}$) with a magnetic moment of $\sim 1.9 \mu B$ per chromium atom with a Neel temperature, $T_N$, of about 240 K. However, in their susceptibility measurements they did not observe any clear maximum indicative of a transition temperature from paramagnetic to a long-range antiferromagnetic ordering

[1,3]. Chamberland and Moeller [4] also synthesized $PbCrO_3$ and their structural results were in agreement with the previous ones, but in addition, reported an unusual broadening of the diffraction peaks even using monochromatic $CuK\alpha 1$ radiation. These broad lines in the X-ray powder patterns were also observed for the same compound by Goodenough et al. [5]. However, in these works neither atomic concentration nor microstructural studies were considered and/or analyzed.

It is well known that the $Pb^{2+}$ $6s^2$ lone pair in some perovskites results in disorder of this cation as confirmed by a high thermal factor in XRD refinements [6], and assignment to a general position by displacement of this cation.

A rather puzzling situation concerning the $3d$ metal ($4+$) lead-based perovskites resides in the fact that while $PbTiO_3$ is tetragonal with $c/a = 1.064$ and ferroelectric with $T_c \sim 763 K$ [7], and $PbVO_3$ is also tetragonal with a higher tetragonality factor, $c/a = 1.229$ [8,9], $PbCrO_3$ has been described as cubic. This is unexpected as in terms of ionic size the following trend is observed: $^{VI}r_{Cr}^{4+} < {}^{VI}r_{V}^{4+} < {}^{VI}r_{Ti}^{4+}$ (0.55, 0.58, and 0.605 Å, respectively) [10]. Thus, one could expect that $PbCrO_3$ should be even more tetragonal since the Cr(IV)–O bond would be more covalent.

Electron microscopy and electron diffraction are often used to solve structural details that XRD cannot resolve [11–14], and in the case of other lead perovskites,

---

*Corresponding author.
E-mail address: maaf@quim.ucm.es (M.A. Alario-Franco).

microstructural studies have helped solve the real structures [15]. From this point of view, we have performed a structural and microstructural study using XRD, selected area electron diffraction (SAED) and high-resolution transmission electron microscopy (HRTEM) to elucidate the origin of the abnormal broadening of the XRD maxima and to clarify the origin of the cubic structure of $PbCrO_3$. In this way, it is shown that the lead-perovskite compound "$PbCrO_3$" has a Pb deficiency, resulting in a modulated structure within a complex microdomain texture.

## 2. Experimental

$PbCrO_3$ was synthesized in a high-pressure "belt"-type apparatus at 1073 K and 80 kbars from stoichiometric amounts of high purity PbO and $CrO_2$. The reaction products, formed after 0.5–1 h, were quenched to room temperature prior to the release of pressure.

Powder XRD experiments were performed on an X'Pert PRO ALPHA 1 (Panalytical) instrument with a germanium monochromator ($CuK\alpha1 = 1.54056$ Å). XRD data were collected with a step of $0.033°$ from $10°$ to $110°$ $2\theta$, over a period of 12 h. Structural refinements were undertaken using the Rietveld program Fullprof [16].

For transmission electron microscopy (TEM), the samples were prepared by grinding the powder, dispersed in $n$-butyl alcohol and a few drops of the suspension collected on a holey carbon-coated copper grid. SAED was performed for the microstructural characterization with a JEOL JEM FX2000 microscope, equipped with a double tilt $\pm 45°$ holder, working at 200 kV. HRTEM was carried out on a JEOL JEM 3000FEG microscope, with $C_S = 0.6$ nm, operating at 300 kV. HRTEM multislice image simulations were carried out using the EMS suite of programs [17].

## 3. Results and discussion

### 3.1. X-ray powder diffraction

Experimental, calculated, and difference XRD patterns are shown in Fig. 1. The analysis of these data is consistent with the perovskite structure and space group $Pm\bar{3}m$, as previously reported [2–5]. The sample used for the structure refinement contains additionally small amounts of PbO, $Cr_2O_3$, and $Pb_5CrO_8$. Structural information for PbO, $Cr_2O_3$, and $Pb_5CrO_8$ were taken from Refs. [18–20], respectively. The background was corrected by means of linear interpolation between given points, while the peak shape for the principal phase was described by a Thompson–Cox–Hastings pseudo-Voigt convoluted with axial divergence asymmetry function [21] and for impurity phases by pseudo-Voigt profiles. For impurity phases, only the unit cell and profile parameters were refined. Cell parameters, atomic coordinates, weight percentages and thermal factors obtained by Rietveld treatment for $PbCrO_3$ are listed in Table 1.
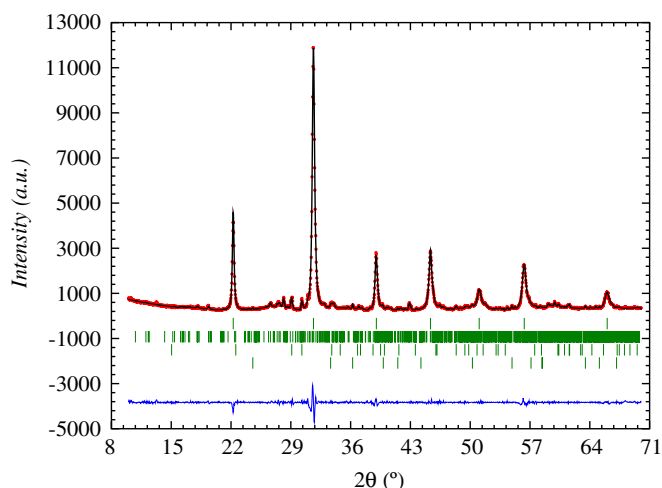


Fig. 1. Experimental, calculated, and difference X-ray patterns for $PbCrO_3$. Peak positions for $PbCrO_3$ (up), $Pb_5CrO_8$, PbO, and $Cr_2O_3$ (bottom) are indicated.

In a first step, the atoms were fixed at their special Wyckoff positions, i.e. Pb ($1a$) $(0, 0, 0)$, Cr ($1b$) $\left(\frac{1}{2}\ \frac{1}{2}\ \frac{1}{2}\right)$ and O ($3c$) $\left(0\ \frac{1}{2}\ \frac{1}{2}\right)$. With this choice, the refined thermal motion parameter of Pb for the $PbCrO_3$ was abnormally large ($B_{Pb} = 1.953(3)$ Å$^2$), indicating the likely presence of structural disorder [22]. The nature of the Jahn–Teller effect in $^{VI}Cr(4+)$, a cation with two unpaired electrons located in the three $t_{2g}$ orbitals, appears to be negligible [23] and often results in undistorted $[CrO_6]$ octahedra [24,25].

Structural disorder of lead is a common feature of most Pb-based complex perovskites (e.g. $Pb_2CoWO_6$, $Pb_2MgTeO_6$, $Pb_2MgWO_6$, $PbSc_{0.5}(Ti_{0.25}Te_{0.25})O_6$, $PbFe_{0.5}Ta_{0.5}O_3$, $Pb_2ScTaO_6$, $PbSc_{0.5}Nb_{0.5}O_3$, and $PbMg_{0.33}Nb_{0.67}O_3$) [26–33], where lead is not on the special Wyckoff position, but statistically split over several neighboring sites. For example, in $PbFe_{0.5}Nb_{0.5}O_3$ the neutron diffraction refinement gives a $B_{Pb} = 3.68(3)$ Å$^2$ for $Pb^{2+}$ in position ($1a$) [22], but for $Pb_2MgWO_6$ $B_{Pb} = 2.87(2)$ Å$^2$ can be reduced to $B_{Pb} = 0.9(2)$ Å$^2$ if the Pb is split over the $12i$ position and displaced 0.259(8) Å along the $\langle 110 \rangle$ [33].

With this in mind, the possibility of the disordered behavior of the Pb site ($1a$) in $PbCrO_3$ was investigated, with three types of disorder models considered where displacements was along the $\langle 100 \rangle$, $\langle 110 \rangle$, and $\langle 111 \rangle$ directions, these correspond to splitting over ($6e$), ($12i$), and ($8g$) positions, respectively. The Pb positions were fixed step by step and the remaining parameters were refined. Fig. 2 shows the agreement coefficients $R_{Bragg}$ and $R_f$ of the Rietveld refinement plotted as a function of the Pb shift from the ideal position for these three kinds of disorder. It can be seen that the three models are equally probable and they all find a minimum for the same displacement from the special Wyckoff position, suggesting that the lead is distributed over a sphere with a radius equal

Table 1
Crystal data, isotropic displacement parameters (Å$^2$) and reliability factors for PbCrO$_3$

| Formula | | | | | | PbCrO$_3$ |
|---|---|---|---|---|---|---|
| Crystal system | | | | | | Cubic |
| Space group | | | | | | $Pm\bar{3}m$ |
| Cell parameter, Å | | | | | | 4.002 (1) |
| Volume, Å$^3$ | | | | | | 64.096 (3) |
| Background | | | | | | Linear interpolation |

| Phase | PbCrO$_3$ | | PbO | | Pb$_5$CrO$_8$ | Cr$_2$O$_3$ |
|---|---|---|---|---|---|---|
| $R_{Bragg}$, $R_f$ | 0.059, 0.030 | | 0.071, 0.029 | | 0.092, 0.054 | 0.060, 0.028 |
| wt% | 87.2 | | 2.4 | | 5.1 | 5.3 |

| Atom | Wyckoff position | $x$ | $y$ | $z$ | Biso (Å$^2$) |
|---|---|---|---|---|---|
| Pb | 1$a$ | 0 | 0 | 0 | 1.953 (3) |
| Cr | 1$b$ | $\frac{1}{2}$ | $\frac{1}{2}$ | $\frac{1}{2}$ | 1.14 (8) |
| O | 3$c$ | 0 | $\frac{1}{2}$ | $\frac{1}{2}$ | 0.6 (2) |

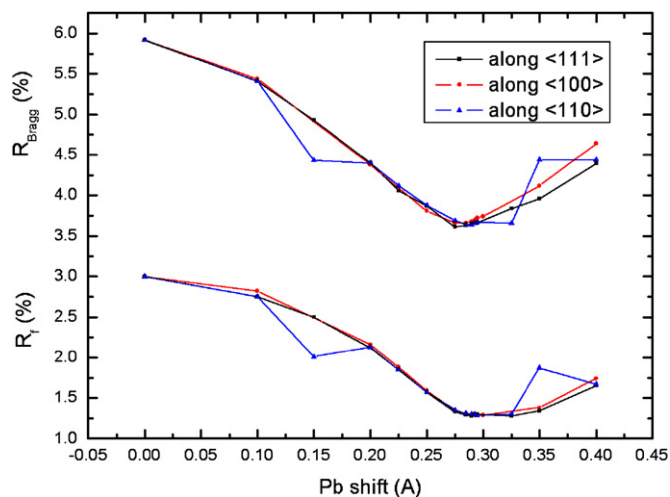$R_{wp} = 9.37\%$, $R_{exp} = 4.68\%$, and $R_p = 6.90\%$.



Fig. 2. $R_{Bragg}$ and $R_f$ versus the Pb shift for the average cubic phase of PbCrO$_3$ from the X-ray powder diffraction data. The three models show the same minimum.



Fig. 3. An approximate representation of the average structure of PbCrO$_3$ as suggested by X-ray diffraction: Cr seats in regular oxygen octahedron while lead is distributed over a multi-splitted $A$ position.

to $r \approx 0.29$ Å. Fig. 3 shows this average cubic structure of the perovskite, where the lead atom is split over different equivalent sites within the cubo-octahedral void among the (CrO$_6$) octahedra. Although this result is consistent with the anomalous lead thermal factor observed, further investigation by electron microscopy was required to correlate the average X-ray structure with microstructural features.

### 3.2. Electron microscopy and diffraction

Fig. 4 shows different SAED patterns of PbCrO$_3$ in which the Bragg reflections have been indexed according to the ideal perovskite cell. All the zone axes present diffuse scattering in the form of streaks that is characteristic of modulated structures arising from periodic perturbations or modulations of the basic cell. This diffuse scattering
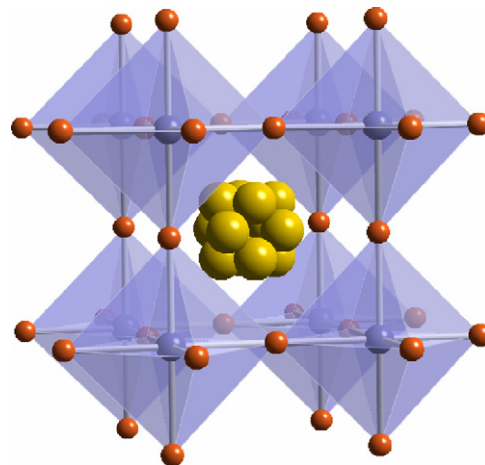
occurring at any position in reciprocal space can be defined by a wave vector $G_p \pm q$, where $G_p$ is a reciprocal lattice vector of the perovskite-type lattice and $q$ is a modulation vector.

The pattern corresponding to the $[001]_p$ zone axis (where the subindex $p$ refers to the basic perovskite cell), Fig. 4a, is illustrative, and shows besides the characteristic maxima of the basic cubic perovskite, elongated diffuse intensity maxima (streaks) at $G_p \pm 1/3\langle 1\gamma 0 \rangle^*$ and $G_p \pm 1/3\langle \delta 10 \rangle^*$ with $\gamma, \delta \in (-1/2, 1/2)$ perpendicular to the three $\langle 001 \rangle^*$ directions running through all the $Pm\bar{3}m$ average structure Bragg reflections $G_p$. Small angle tilting (Figs. 4b–d) around the main reciprocal axis did not move or shorten the streaks, showing that these satellite reflections are part of sheets of diffuse intensity. This allows construction of a three-dimensional representation of the reciprocal lattice as shown in Fig. 5.
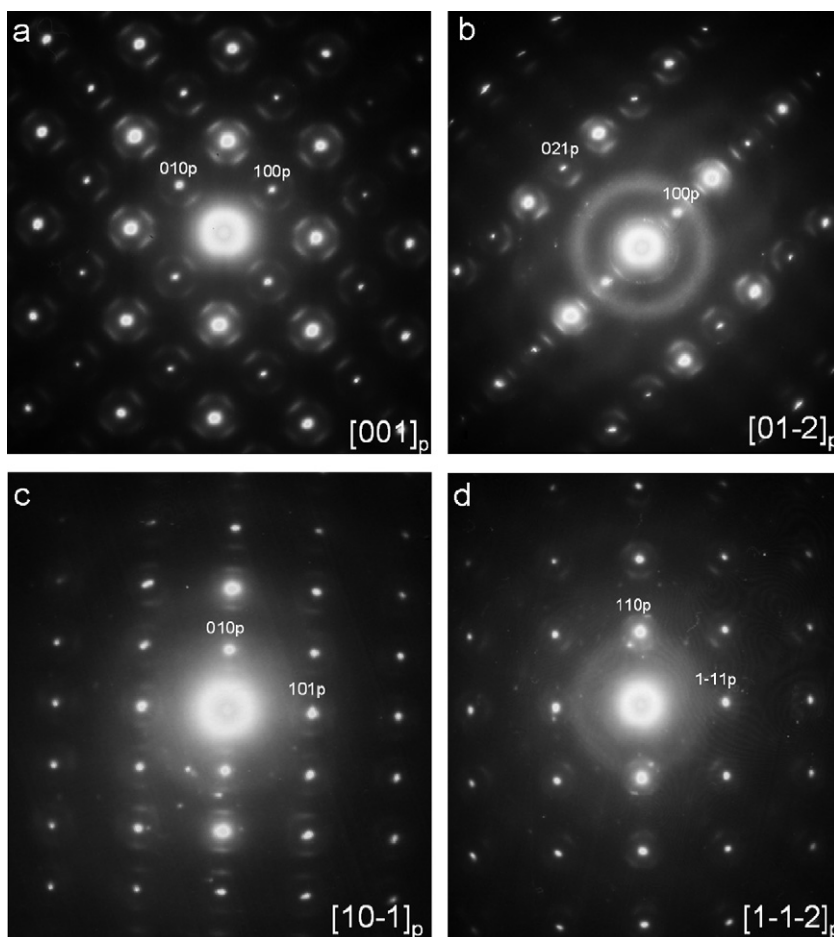
Fig. 4. SAED patterns of PbCrO$_3$ along the (a) $[001]_p$, (b) $[01\bar{2}]_p$, (c) $[10\bar{1}]_p$, and (d) $[1\bar{1}\bar{2}]_P$ zone axes. (Subindex $p$ refers to the basic perovskite cell.)

These streaks could be due to a disordered modulation in real space. Taking into account that the correlation length along one direction is inversely proportional to the length of the diffuse scattering along that direction in reciprocal space, the size of the streaks allows an estimation of the dimensions of the modulation.

The important difference in information gathered with X-ray powder diffraction and electron diffraction is due to the difference in coherent length and interaction intensity, which are more favorable for electrons [34]. The streaks can be attributed to the intersection of the Ewald sphere with diffuse scattering sheets. These sheets are placed at $(1/3)a_p^*$ from the main reflections, defined by $G_p \pm 1/3\langle 1\gamma\delta\rangle^*$ along the three $\langle 001\rangle^*$ directions (Fig. 5b). The presence of planes of diffuse scattering in reciprocal space reflects the existence of linear disorder in real space along certain atomic chains in the direction perpendicular to the diffuse plane. There is a somewhat similar situation in the case of $\beta$-cristobalite [35] and in BaTiO$_3$ [36].

Fig. 6 shows a $[001]_p$ high-resolution micrograph of PbCrO$_3$; besides the expected cubic perovskite fringes, regions of different contrast are observed creating of a patch-work array. In some regions, $\sim 12$ Å wide fringes are parallel to $g_{100p}$ (reciprocal vector along $[100]_p^*$ direction),
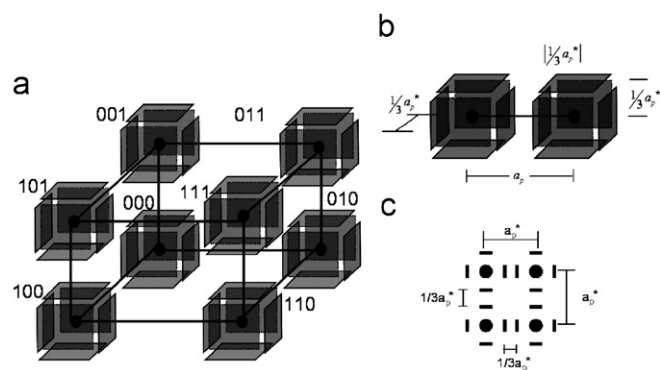


Fig. 5. (a) Perspective drawing of the reciprocal lattice for PbCrO$_3$ showing diffuse diffraction effects in the form of sheets surrounding each principal maximum as they are observed to occur in the electron diffraction patterns. (b) The sheets of diffuse scattering are placed at $1/3a_p^*$ in the three main principal directions. (c) Expected electron diffraction pattern along [001], cf. Fig. 4a.

while in other regions similar fringes align with $g_{010p}$, which suggests the presence of microdomains (Fig. 6a). The fast Fourier transform (FFT) of this image shows the diffuse intensity (Fig. 6b), in agreement with the experimental diffraction pattern (Fig. 4a). In order to better understand
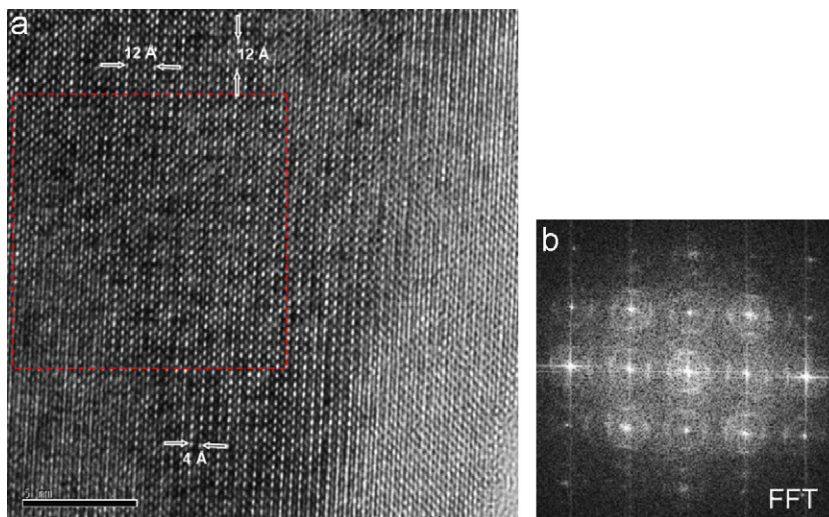
Fig. 6. (a) HRTEM image along the $[001]_p$ zone axis for $PbCrO_3$. (b) Fourier transform of the remarked zone.
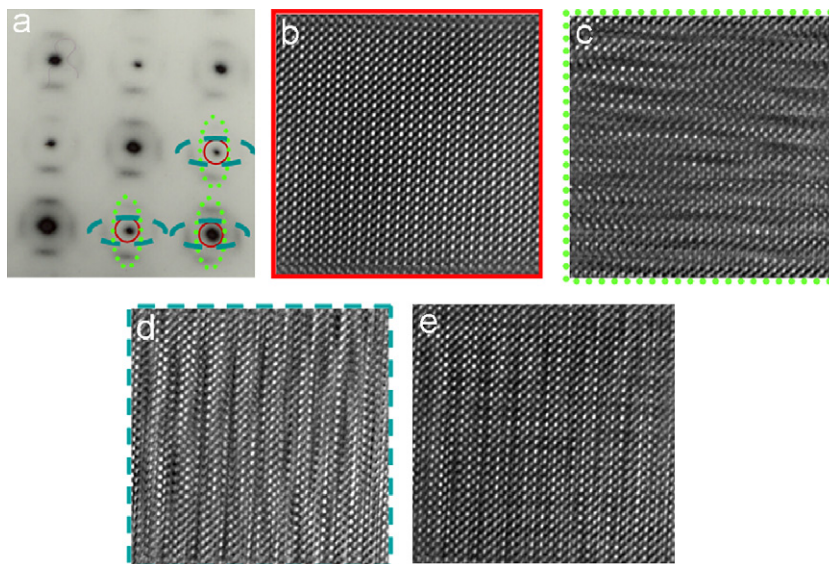


Fig. 7. (a) Schematic representation of the masks applied over the FT to process the images. (b) Image reconstructed just considering the principal maxima. (c, d) Idem considering besides the principal maxima, the streaks along one direction. (e) Sum of (b)–(d) compare with Fig. 6a (see text).

the origin of these features, masks were applied over the FFT patterns [37]. By considering just the principal maxima of Fig. 7a, the cubic perovskite subcell is returned (Fig. 7b). To emulate the microdomains, the IFFT of the satellites along one direction was added five times to the corresponding IFFT of the perovskite. It is observed that the intensities of the white dots along the direction of the streaks are modulated; this behavior is also obeyed in the perpendicular direction (Fig. 7d). The addition of the three filtered images ($7a + 7b + 7c$), recover an image (Fig. 7e) that agrees well with experiment (Fig. 6a). Therefore, it is postulated that the real crystal is constructed from the intergrowth of two modulated domain sets, parallel to $g_{100p}$ and $g_{010p}$. In addition, tilting experiments show that in reciprocal space there is diffuse scattering sheets along a

third direction, $1/3g_{001p}$ above the Ewald sphere (Fig. 5b), that not contribute to the images shown in Figs. 6a–8.

Considering just the streaks in one direction in the FFT, say $a^*$ without the principal spots and filtering, a modulation is revealed in the rows along [100] (Fig. 8a) with a periodicity ($T$) that varies between $\sim 14a_p$ and $\sim 18a_p$ (Fig. 8b) and a phase shift $\phi = T/3$ in the [010] direction (periodicity of $3a_p$ along $b$) (Fig. 8c), that corresponds to one domain set.

EDX analysis was performed over 15 crystals of three different samples; statistically, the atomic Pb:Cr ratio was determined to be 0.91(5):1. These results and the observed modulation, suggest $A$-site vacancy ordering [12–14,38,39]. From XRD refinement, a mass balance based on the weight percentages of the impurities results in a Pb
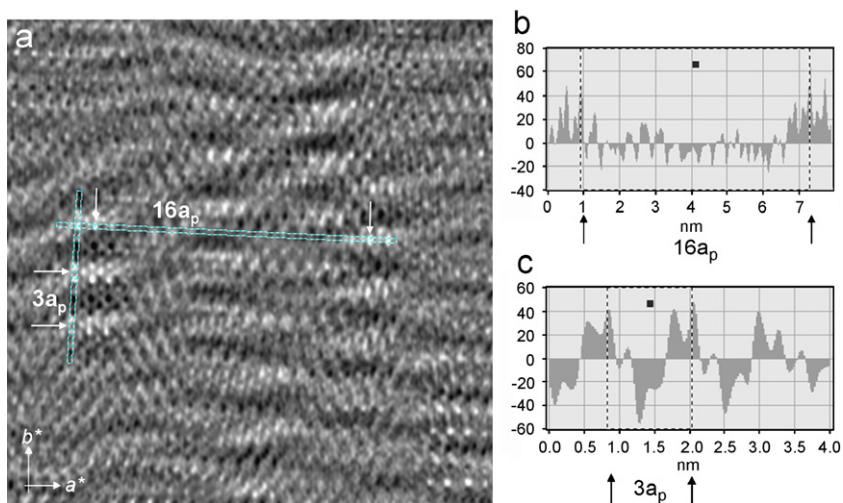
Fig. 8. (a) Filtered image obtained from the FFT, shown in Fig. 4b, by placing masks on the diffuse scattering steaks along the $a^*$ direction only. (b) Intensity profile along the $[100]_p$ that shows the modulation of the intensities with a period $M \approx 16a_p$ (between the maxima of intensity) along $a^*$. (c) Intensity profile along the $[010]_p$ direction showing that the periodicity of the spots along $b^*$ its equal to $3a_p$.

deficiency in the main phase with a Pb:Cr ratio of $\sim 0.86:1$ in agreement with the direct measure by EDX. Therefore, the chemical formula is best expressed as $Pb_{1-x}CrO_{3-x}$ with $x \approx 0.1$ and with the oxidation state of chromium entirely tetravalent. This implies that some chromium atoms would be in a tetrahedrally coordinated, as this is not unusual for $Cr^{IV}$ [10], however the presence of $Cr^{III}O_6$ polyhedra cannot be ruled out. In some compounds, Cr(III) and Cr(IV) co-exist [40–45] and this maybe true in the present case.

The displacement of the Pb atom obtained by Rietveld refinement of the XRD data is not in contradiction with a cationic compositional modulation, as these are commonly accompanied by displacive modulation [12–14]. Although, under optimal conditions, the atomic coordinates can be directly estimated from HREM images [46–48] the interference of the three sets of domains observed here prevents such an analysis.

### 3.3. A model for the modulation

In order to establish a model for the compositional modulation lead is considered to be located on its special position. With this assumption, a model with $T = 16a_p$ is proposed. The modulation of the occupation factor of the $Pb^{2+}$ cations may be expressed in general terms as

$$f(y,z) = A + B\cos^2\left(\frac{\pi z}{T} + \phi(y)\right), \qquad (1)$$

where $z$ is the position of the $Pb^{2+}$ cations along the direction of the modulation, $T$ the period of the sinusoidal modulation, $\phi(y)$ the phase change between the different atomic planes along $b$ sustaining the modulation, and $A$ and $B$ are constants to be determined.

To calculate $A$ and $B$, can be related by two equations [49,50]. The first one is obtained by defining the average

value of the function $f(z)$, i.e. the average occupation of the $Pb^{2+}$ cations in the planes of the modulation:

$$\langle f(z) \rangle = \frac{1}{T} \int_0^T f(z)\,\mathrm{d}z = \text{average occupation} \qquad (2)$$

solving the integral one obtains

$$A + B/2 = \text{average occupation}. \qquad (3)$$

The second equation results from fixing the degree of occupation of the position considered as origin of the modulation, whose coordinate is $z = 0$, and which is normally given by the maximum value of the occupation:

$$A + B = \text{fixed degree of occupation}. \qquad (4)$$

Therefore, the average composition of $Pb^{2+}$ cations in the modulation planes is required. According to EDX analysis and considering that each layer has the same lead composition, the average occupation is equal to 0.91 so

$$A + B/2 = 0.91 \text{ and } A + B = 1, \ A = 0.82, \ B = 0.18.$$

Since there is a change in phase between the planes, $\phi(y) = (T/3)y$, the modulation function along one direction in the "$PbCrO_3$" is

$$f(x,y) = 0.82 + 0.18\cos^2\left(\frac{\pi x}{64} + \phi(y)\right). \qquad (5)$$

For the simulation of the image, based on the proposed modulation, we considered an orthorhombic supercell $a_p \times 3a_p \times 16a_p$ with a defocus value of $-55$ nm and a crystal thickness of 3.6 nm (Fig. 9a). The occupation for each Pb used in the simulation, as calculated from Eq. (5), is plotted in Fig. 9b considering the interlayer phase shift. The superposition of this simulated image to the experimental one that is filtered shows good agreement with the observations (Fig. 10), at least for the number of cells considered.
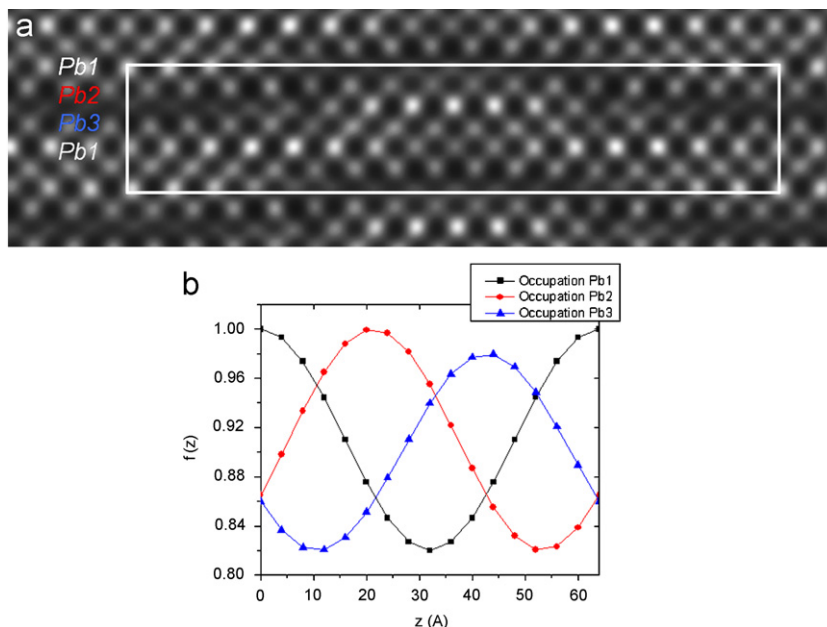
Fig. 9. (a) Calculated HRTEM image along $[100]_p$ based on the occupational modulation model proposed for "PbCrO$_3$" (b) Occupation factor of lead along the supercell showing the interlayer phase shift.
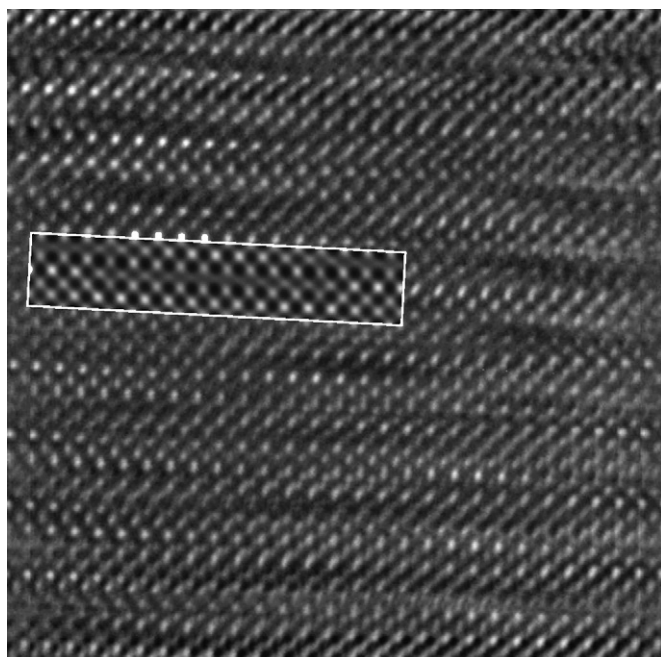


Fig. 10. Superposition of the Inverse FFT considering the principal maxima and the streaks along one direction and the simulated image (white frame) obtained with the model of compositional modulation. It is clear the similarity between them.



Fig. 11. Calculated electron diffraction pattern along the $[100]_p$ based on the occupational modulation model of the PbCrO$_3$ (see text for details).

Fig. 11 shows the calculated electron diffraction pattern for the proposed model along $[100]_p$. This zone axis corresponds to that in Fig. 4a. In the calculated electron diffraction patterns the diffuse streaks are clearly observed at $G_p \pm 1/3\langle 01\gamma \rangle^*$. These "streaks" are composed of dots instead of continuous lines of intensity, because they are simulated only for $T = 16a_p$, whereas, the real diffraction pattern is a consequence of the disorder in the
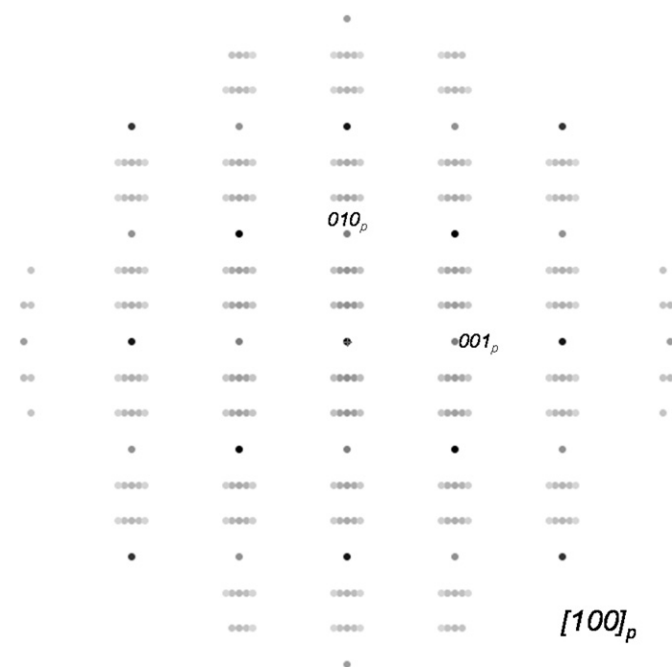
modulation with variable periodicities $T \approx 14$–$18a_p$. This model provides an explanation for the streaks, but not to the sheets of diffuse scattering obtained in the reconstruction of the reciprocal lattice (Fig. 5), which arise from lack of correlation of the modulation between nearest cells. The intergrowth of three sets of microdomains justifies the presence of the other two sheets, along [010] and [001].
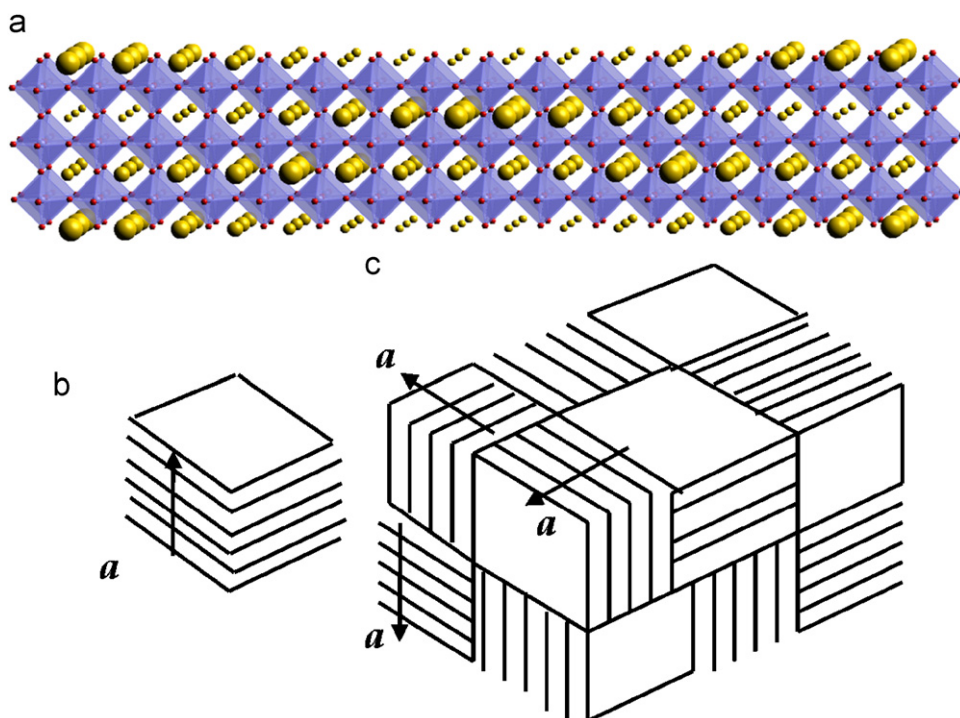
Fig. 12. (a) Model of the structure of PbCrO$_3$ obtained by electron microscopy and diffraction. The occupation factor of the Pb atoms has been scaled so as to make it more clearly visible. Lead is yellow, chromium is purple and oxygen is red (color online). (b) Single domain of a schematic representation of the microdomain texture of "PbCrO$_3$". (c) Intergrowth of domains in different orientations.

### 3.4. Description of the structure of "PbCrO$_3$"

Although the *average* basic structure of PbCrO$_3$, as observed by powder XRD, *appears cubic*, lead occupation is split over 26 sites, (Fig. 3), and the *real structure* can be described as an incommensurate superlattice. This can be described as a compositional modulation of the Pb atoms with a periodicity ($\sim$14–18$a_p$) that repeats along the *b*-axis every three perovskite cells, so that the true unit cell is $a_p \times 3a_p \times (\sim 14$–$18)a_p$. Fig. 12 gives a schematic view of the structure where the radii of the lead represent the approximate occupation of the lead sites distributed along the *c*-axis according to the established modulation (Eq. (5)). A schematic representation of the microdomain intergrowth is shown on Fig. 12c.

### 4. Conclusions

SAED and HRTEM studies of "PbCrO$_3$" reveal that this material is far from being a conventional cubic perovskite. The abnormal broadening of the powder XRD lines is due to a very complex microstructure that arises from a compositional modulation of lead atoms along the three principal directions that creates three sets of microdomains. Assuming a commensurate superstructure with an *average* period of 16 perovskite cells and with a phase shift of $\phi = T/3$, an orthorhombic structure model is proposed $(a_p \times 3a_p \times (\approx 14$–$18)a_p)$. The calculated HRTEM images and electron diffraction patterns based on this modulated structural model, which is due to the periodic variation of the occupation factor of Pb atoms, agrees well with the experimental data. The final conclusion is then that there is not really "PbCrO$_3$", but Pb$_{1-x}$CrO$_{3-x}$ that under the present synthesis conditions has $x = 0.091(5)$.

### References

[1] W.L. Roth, R.C. DeVries, J. Appl. Phys. 38 (1967) 951.
[2] M.A. Alario-Franco, K.S.W. Sing, J. Therm. Anal. Calorim. 4 (1972) 47.
[3] R.C. DeVries, W.L. Roth, J. Am. Ceram. Soc. 51 (1968) 72.
[4] B.L. Chamberland, C.W. Moeller, J. Solid State Chem. 5 (1972) 39.
[5] J.B. Goodenough, J.A. Kafalas, J.M. Longo, in: P. Hagenmuller (Ed.), Preparative Methods in Solid State Chemistry, Academic Press, New York, 1972.

[6] G. Baldinozzi, Ph. Sciau, P. Pinot, D. Grebille, Phys. Status Solidi A 33 (1992) 17.

[7] R.E. Cohen, Nature 358 (1992) 136.

[8] R.V. Sphanchenko, V.V. Chernaya, A.A. Tsirlin, P.V. Chizhov, D.E. Sklovsky, E.V. Antipov, Chem. Mater. 16 (2004) 3267.

[9] A.A. Belik, M. Azuma, T. Saito, Y. Shimakawa, M. Takano, Chem. Mater. 17 (2005) 269.

[10] R.D. Shannon, Acta Crystallogr. A 32 (1976) 751.

[11] M.Á. Alario-Franco, M.V. Regi, Nature 270 (1977) 706.

[12] S. García-Martín, M.Á. Alario-Franco, H. Ehrenberg, J. Rodríguez-Carvajal, U. Amador, J. Am. Chem. Soc. 126 (2004) 3587.

[13] M.Á. Alario-Franco, I.E. Grey, J.C. Joubert, H. Vincent, M. Labeau, Acta Crystallogr. A 38 (1982) 177.

[14] M. Labeau, I.E. Grey, J.C. Joubert, H. Vincent, M.A. Alario-Franco, Acta Crystallogr. A 38 (1982) 753.

[15] G. Baldinozzi, G. Calvarin, Ph. Sciau, D. Grebille, E. Suard, Acta Crystallogr. B 56 (2000) 570.

[16] J. Rodríguez-Carvajal, Physica B 192 (1993) 55.

[17] P. Stadelmann, JEMS, version 20105.

[18] J. Leciejewicz, Acta Crystallogr. 14 (1961) 66.

[19] L.W. Finger, R.M. Hazen, J. Appl. Phys. 51 (1980) 5362.

[20] S.V. Krivovichev, T. Armbruster, W. Depmeier, J. Solid State Chem. 177 (2004) 1321.

[21] L.W. Finger, D.E. Cox, A.P. Jephcoat, J. Appl. Crystallogr. 27 (1994) 892.

[22] N. Lampis, Ph. Sciau, A. Geddo Lehmann, J. Phys. Condens. Matter 11 (1999) 3489.

[23] F.A. Cotton, G. Wilkinson, P.L. Gaus, Basic Inorganic Chemistry, Wiley, Inc., Canada, 1995.

[24] P. Porta, J.P. Remeika, M. Marezio, P.O. Dernier, Mater. Res. Bull. 7 (1972) 157.

[25] R. Ruíz-Bustos, M.H. Aguirre, M.Á. Alario-Franco, Inorg. Chem. 44 (2005) 3063.

[26] G. Baldinozzi, Ph. Sciau, J. Lapasset, Phys. Status Solidi A 133 (1992) 17.

[27] G. Baldinozzi, D. Grebille, Ph. Sciau, J.M. Kiat, J. Moret, J.F. Bérar, J. Phys.: Condens. Matter 10 (1998) 6461.

[28] G. Baldinozzi, Ph. Sciau, M. Pinot, D. Grebille, Acta Crystallogr. B 51 (1995) 668.

[29] J.A. Alonso, I. Rasines, J. Phys. Chem. Solids 49 (1988) 385.

[30] A. Geddo Lehmann, F. Kubel, H. Schmid, J. Phys.: Condens. Matter 9 (1997) 8201.

[31] S.G. Zhukov, V.V. Chernyshev, L.A. Aslanov, S.B. Vakhrushev, H. Schenk, J. Appl. Crystallogr. 28 (1995) 385.

[32] C. Malibert, B. Dkhil, J.M. Kiat, D. Durand, J.F. Bérar, A. Spasojevid-de Biré, J. Phys.: Condens. Matter 9 (1997) 7485.

[33] A. Verbaere, Y. Piffard, Z.G. Yé, E. Husson, Mater. Res. Bull. 27 (1992) 1227.

[34] W. Massa, Crystal Structure Determination, Springer, Berlin, 2004.

[35] R.L. Withers, J.G. Thompson, T.R. Welberry, Phys. Chem. Min. 16 (1989) 517;
R.L. Withers, Z. Kristallogr. 220 (2005) 1027.

[36] R. Comés, L. Lambert, A. Guinier, Acta Crystallogr. A 26 (1970) 244.

[37] I. Levin, L.A. Bendersky, T.A. Vanderah, Philos. Mag. A 80 (2000) 411.

[38] I. Levin, T.A. Vanderah, T.G. Amos, J.E. Maslar, Chem. Mater. 17 (2005) 3273.

[39] P.D. Battle, J.E. Bennet, J. Sloan, R.J.D. Tilley, J.F. Vente, J. Solid State Chem. 149 (2000) 360.

[40] M.Á. Alario-Franco, J.M. Thomas, R.D. Shannon, J. Solid State Chem. 9 (1974) 261.

[41] B.L. Chamberland, C.G. Frederick, J.L. Gillson, J. Solid State Chem. 6 (1973) 561.

[42] D.P. Karim, A.T. Aldred, Phys. Rev. B 20 (1979) 2255.

[43] S. Miyazaki, S. Kikkawa, M. Koizumi, Rev. Chim. Min. 19 (1982) 301.

[44] J.J. Neumeier, Hirotoshi Terashita, Phys. Rev. B 70 (2004) 214435.

[45] E. Cuno, Hk. Müller-Buschbaum, Z. anorg. Allg. Chem. 572 (1989) 175.

[46] T. Oku, A. Carlsson, L.R. Wallenberg, J.-O. Malm, J.-O. Bovin, I. Higashi, T. Tanaka, Y. Ishizawa, J. Solid State Chem. 135 (1998) 182.

[47] T.E. Weirich, R. Ramlau, A. Simon, S. Hovmoëller, X. Zou, Nature 382 (1996) 144.

[48] T. Oku, S. Nakajima, J. Mater. Res. 13 (1998) 1136.

[49] M. Labeau, Ph.D. Thesis, 1980, Grenoble, France.

[50] M.A. Señaris-Rodriguez, M.A. Alario-Franco, S. Stoll, A.M. Stacy, Physica C 282 (1997) 801.